Monte Carlo Simulation of Radiation Trapping in Hg–Ar Fluorescent Discharge Lamps

M. Baeva[1] and D. Reiter[1,2]

The line spectra of emitted resonance radiation from mercury and the effective decay rates of the Hg 6^3P_1 and 6^1P_1 levels in mercury–argon discharges are simulated by a Monte Carlo method. The hyperfine splitting, the natural isotopic composition, collisional transfer of excitation, foreign gas collisions and quenching are considered to describe in detail the 253.7 nm and 184.9 nm lines. The calculations are performed for Hg vapor densities corresponding to coldest spot temperatures of 5–100°C, and discharge parameters typical for fluorescent lamp operation. The densities of the Hg 6^3P_1 and 6^1P_1 levels are consistently estimated by means of a set of balance equations for the Hg 6^3P_0, 6^3P_1, 6^3P_2, and 6^1P_1 excited states. The resulting uv radiation output of the discharge is then estimated for a tube radius of 18 mm, argon pressure of 400 Pa, discharge current 0.4 A, and wall temperatures of 20–80°C. The results obtained show a good agreement as compared with published experimental data.

1. INTRODUCTION

The resonance radiation from mercury is frequently used for lighting applications in low-pressure fluorescent lamps. Mercury atoms excited to the 6^3P_1 and 6^1P_1 states emit ultraviolet radiation at 253.7 nm and 184.9 nm respectively in decaying to the 6^1S_0 ground state (see Fig. 1). Due to opacity many emission-absorption steps are required before the radiation reaches the phosphor-coated discharge wall. Typical discharge conditions fall into the intermediate region between optically thick and optically thin limits.

A detailed review of resonance radiation transport simulation is given in Ref. 1. The authors describe the three principal approaches to modeling

[1]Institute of Laser and Plasma Physics, Heinrich-Heine-University of Düsseldorf, Universitätsstr. 1, D-40225 Düsseldorf, Germany.
[2]Institut für Plasmaphysik, Forschungszentrum Jülich GmbH, EURATOM Association, Trilateral Euregio Cluster, D-52425 Jülich, Germany.
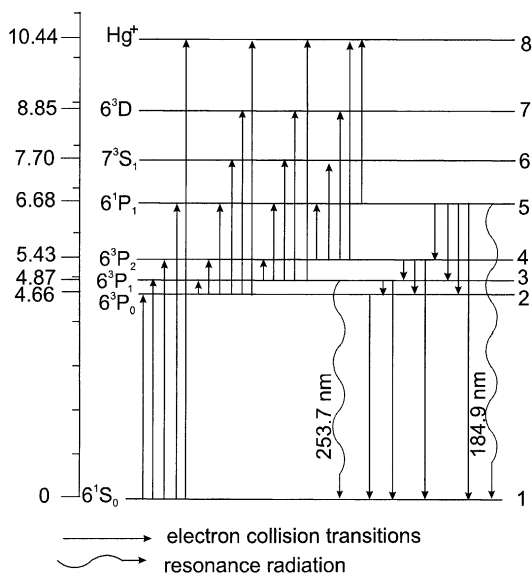
Fig. 1. Energy level diagram of mercury atom.

of radiation transfer: the Holstein–Biberman equation, the method of combining the equation of radiative transfer with the rate equation for the excited atomic states, and the multiple-scattering representation. Furthermore, an extended overview of numerical techniques is provided. These approaches consider the trapping from different points of view but, all describing the same physical process, are equivalent. Biberman[2] and Holstein[3] treated the problem assuming complete frequency redistribution (CFR), i.e., without any correlation between the frequency of an absorbed photon and that of the photon emitted subsequently. This approach was further expanded[4] to include the effects of partial frequency redistribution (PFR), and applied to "early time" decay[4] and the "late time" decay[5] of the fundamental mode. The multiple-scattering representation computes the probabilities for photons to escape after absorption/re-emission processes. A common way to obtain these probabilities is based on Monte Carlo simulations. The photon's emission frequency, direction, and free flight distance before reabsorption are taken at random, according to the appropriate probability distributions, and fulfilling the statistics of the physical processes under consideration.

Monte Carlo simulations of radiation transport with CFR and PFR are reported in Refs. 6 and 7. The imprisonment of the 253.7 nm resonance

radiation from mercury in Hg–Ar discharge fluorescent lamps was studied in Refs. 6 and 8. The emission lineshapes as affected by Doppler and pressure broadening[9] were taken into account. Of particular interest was the isotopic mercury content, as well as the effect of an external applied magnetic field, which had influence on the emission lineshape, and thereby on the fluorescent lamp efficiency.

PFR becomes important for very short-lived radiating species such as the 184.9 nm resonance line of mercury.[5,10] An increase in power density in the plasma can increase the ratio of 184.9 to 253.7 nm output, and can consequently affect both the efficiency and the lifetime of fluorescent lamps. Therefore, a better understanding of the transport of the 184.9 nm radiation in Hg–Ar discharges is an important issue for modeling and diagnosing lamp discharges. The effects of foreign gas broadening are included in Ref. 10 to randomize the excitation across the hyperfine components of an odd isotope.

In this work we report results obtained from Monte Carlo simulations of the radiation transport of the resonance lines of mercury at 253.7 and 184.9 nm. Distinct from earlier approaches here a more complete set of elementary process channels is studied. In particular the effects of hyperfine and isotopic structure, excitation transfer, and foreign gas broadening are considered to get a more realistic description of the physical processes in Hg–Ar discharges. We compare our results with experimental data published for the effective decay rates of the levels 6^3P_1 and 6^1P_1 in Hg, and Hg–Ar discharges with tube radii of 18 and 12.5 mm. By means of the calculated effective lifetimes of the levels 6^3P_1 and 6^1P_1 we solve a system of balance equations for the $6^3P_{0,1,2}$ and 6^1P_1 excited states of mercury to determine their population densities, and then to estimate the uv radiation output of the discharge. The results obtained for a tube radius of 18 mm in Hg–Ar discharges with Ar pressure of 400 Pa, a discharge current of 0.4 A, and a varying number density, are compared with published experimental data.

2. MONTE CARLO SIMULATIONS

The Monte Carlo simulations are quite conventional[11] and only briefly summarized here. They follow the algorithm as described below. Photons are launched from a specified spatial density distribution of emitters with a frequency chosen at random from the overall lineshapes for the 253.7 nm or 184.9 nm resonance line. The selection of the initial isotopic is made with weighting according to the relative concentrations of each species (see Table I). The direction of emission is selected from three-dimensional

Table I. Stable Mercury Isotopes, Their Natural Abundance and Hyperfine Components of the 253.7 nm and 184.9 nm Line

Mass number (amu)	Abundance Refs. 21, 22	Hyperfine splitting relative to ^{198}Hg in GHz (253.7 nm[23])	Hyperfine splitting relative to ^{198}Hg in GHz (184.9 nm[24,25])
196	0.0015	4.347	3.852
198	0.0997	0	0
199A	0.0562	−15.379	3.034
199B	0.1125	6.715	−2.327
200	0.2310	−4.826	−4.31
201a	0.0659	−14.629	−3.76
201b	0.0439	−0.689	−7.46
201c	0.0220	6.895	−8.72
202	0.2986	−10.132	−9.23
204	0.0687	−15.319	−14.07

isotropic distribution. The length l of the free flight of the photon before being reabsorbed is sampled according to

$$l = -\frac{\ln w}{\sum_i k_i(v)},$$
(1)

where $k_i(v)$ is the absorption of the isotope i, and w is a uniform random number in the interval $(0, 1)$, i.e., the distribution of l is

$$f(l)\, dl = \left(\sum_i k_i(v)\right) \exp\left[-l \sum_i k_i(v)\right] dl.$$
(2)

The various states of the odd isotopes (see Table I) are treated as independent species. Then the point of reabsorption is calculated. If it lies within the computational volume in radial direction, the position is recorded, and the absorbing species is chosen with a probability proportional to its weight in the sum of absorption coefficients. If the point of reabsorption lies outside, the photon is recorded as escaped, and a new one is started. The procedure is repeated until a given number of photons (or statistical precision) is reached.

Upon absorption by a gas atom, the photon will be either: (a) exchanged with another absorbing atom which may be a different isotope, and then re-emitted (resonance collision); (b) re-emitted by the absorbing atom (no collision); (c) re-emitted either from the same isotope (the absorbing atom is an even isotope) or by another hyperfine component (odd isotope) after collision with the foreign gas atom (Ar). The frequency is chosen

from the lineshape of the respective isotope; (d) lost to nonresonant quenching. The choice among the four mechanisms is made according to the probabilities of the respective processes which in turn are related to the rate constants:

$$
\begin{aligned}
&\text{(a)} \quad 0 \leq w \leq P_{rc} \\
&\text{(b)} \quad P_{rc} < w \leq P_{rc} + P_e \\
&\text{(c)} \quad P_{rc} + P_e < w \leq P_{rc} + P_e + P_{fg} \\
&\text{(d)} \quad P_{rc} + P_e + P_{fg} < w \leq P_{rc} + P_e + P_{fg} + P_q = 1.
\end{aligned}
\tag{3}
$$

In (3) w is a uniform random number, and P_{rc}, P_e, P_{fg}, and P_q are the probabilities of resonance collision, emission, foreign gas collision, and quenching, respectively. The probabilities are calculated by the expression

$$
P_i = \frac{R_i}{\sum_j R_j},
\tag{4}
$$

where R_i is the rate constant of the process i ($i = a, b, c, d$).

Such kind of definition of the probabilities was already used in Ref. 6 but the foreign gas collisions (process c) were not considered explicitly when selecting the mechanism channel. Foreign gas broadening was included there in the lineshape only.

Another definition of the probabilities P_i was used in Ref. 10 where the probability of at least one resonance dephasing collision during a vacuum lifetime was computed. If no resonance collision occurred, then the probability of at least one foreign gas collision was calculated. Collisional quenching was not considered as a mechanism channel in Ref. 10 but it was added to the results *a posteriori* of the Monte Carlo simulations.

We make use of the probabilities as given by Eq. (4). The rate constants for resonance and foreign gas collisions are evaluated based on the cross-section and broadening data.[12–15] Resonance collisions randomize the frequency across the Voigt profile of the final component and can change the line component with a probability taken in proportion to their natural abundance. Foreign gas collisions are considered to randomize the frequency across the Voigt profile of the final component. They can change the hyperfine component of odd isotopes. The line component remains the same when the initial excitation is on a line component corresponding to an even isotope. If no collision occurs the frequency of the re-emitted photon in the laboratory frame is determined using appropriate Dopler shifts. Emission frequency generating schemes for angle-averaged and angle-dependent PFR were developed by Lee.[16–18] The angle-dependent redistribution functions were found to provide computational results in better agreement with experimental data. Moreover, the Monte Carlo simulation is no more complicated

for angle-dependent PFR than it is for angle-averaged ones. In the present work the angle-dependent algorithm from Ref. 18 is applied to the resonance transport of the 184.9 nm line of mercury. For the 253.7 nm resonance line of mercury CFR is used because of the large vacuum lifetime of the upper level. Hence, the frequency of the re-emitted photon is generated from the Voigt line profile. In both cases the re-emitted photon has a finite probability of being emitted from the wings of the lineshape where the absorption is lower and the probability for escaping is higher. Since the absorption coefficient varies along the photon trajectory the null collision technique is employed.[19] In selecting the emission frequency from the Voigt lineshape, the approach proposed in Ref. 20 is applied to avoid all numerical integration and "look-up" tables.

3. RESULTS FROM THE MONTE CARLO SIMULATION

The Monte Carlo simulation is carried out to investigate radiation transport, trapping and frequency redistribution in a cylindrical discharge tube filled with mercury vapour and argon. The gas temperature, ground state mercury, and argon density are taken uniformly within the computational volume. The density of the emitters is taken optionally uniform or from a parabolic profile peaked at the axis. The isotopic composition and splitting of mercury lines used in the calculations is given in Table I.

3.1. Transport of Resonance Radiation of the 253.7 nm Line of Hg

Numerous measurements of the naural lifetime of the 6^3P_1 level have been published (see Ref. 28 and the references therein). The value of 120 ns reported in Ref. 28 is used in the present study. The effective decay rates and the emission spectra of the 6^3P_1 level are calculated for mercury densities and tube radii relevant for fluorescent lamps.[6,28,29] The results are presented in Figs. 2–4.

Figure 2 shows the decay rates as a function of the mercury density calculated for a tube radius of 18 mm and argon pressures of 0 and 400 Pa. Experimental data from Ref. 28 are adopted and given for a comparison. Note that in Ref. 28 the data for the effective lifetime of the 6^3P_1 level are presented as a function of k_0R, where R is the tube radius and $k_0 = 2.4 \times 10^{-23}N/(\tau_0 T^{0.5})\text{m}^{-1}$ with N being the mercury ground state density, τ_0– the natural lifetime of the 6^3P_1 level, and T–the absolute temperature. The decay rate for the largest mercury densities is about $2 \times 10^4\,\text{s}^{-1}$, that corresponds to an effective lifetime of the 6^3P_1 level of about 50 μs and agrees well with the measured values in Ref. 28. Cross-sections for collisional quenching $(6^3P_1 \rightarrow 6^3P_0)$ of $\sim 1 \times 10^{-21}\,\text{m}^{2(8)}$ (lower by a factor of ~ 2 than the value reported in Ref. 30), and for collisional broadening by argon atoms of
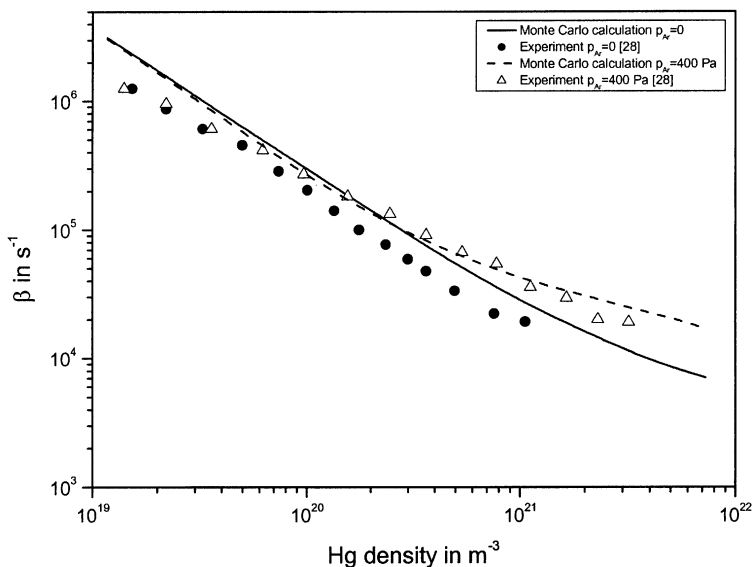
Fig. 2. Effective decay rate of the 6^3P_1 level as a function of the Hg number density. The solid and dashed lines represent the Monte Carlo calculations for a radius R = 18 mm with no buffer gas (solid) and with 400 Pa Ar (dashed). The results are compared with experimental data from Ref. 28.

$3.2 \times 10^{-19}\,\text{m}^2$ (derived from $C_6 = 8.16 \times 10^{-44}\,\text{m}^6/\text{s}$,[14] have been used through the calculations. The cross-section of excitation transfer has been taken as $1.1 \times 10^{-17}\,\text{m}^2$.[31]

Figures 3 and 4 show the results obtained for a tube radius of 12.5 mm. The decay rates of the 6^3P_1 level calculated as a function of the mercury density with no argon and with 400 Pa argon have a similar behavior as those in the case R = 18 mm (Fig. 2). The effective lifetime decreases with decreasing tube radius. The emission spectrum consists of five groups of lines (Fig. 4). At low mercury densities (coldest spot temperature) the emission is determined by the center of the 253.7 nm components and the collisional broadening by argon plays a minor role. With increasing mercury density the effects of radiation trapping may be seen to give an increased line width and line reversal. The wings of the line components become increasingly important and therefore the effect of the foreign gas on the decay rate of the 6^3P_1 level increases.

3.2. Transport of Resonance Radiation of the 184.9 nm Line of Hg

The natural lifetime of the 6^1P_1 level has been reported in numerous publications (see the references given in Ref. 10). We use the value of 1.3 ns
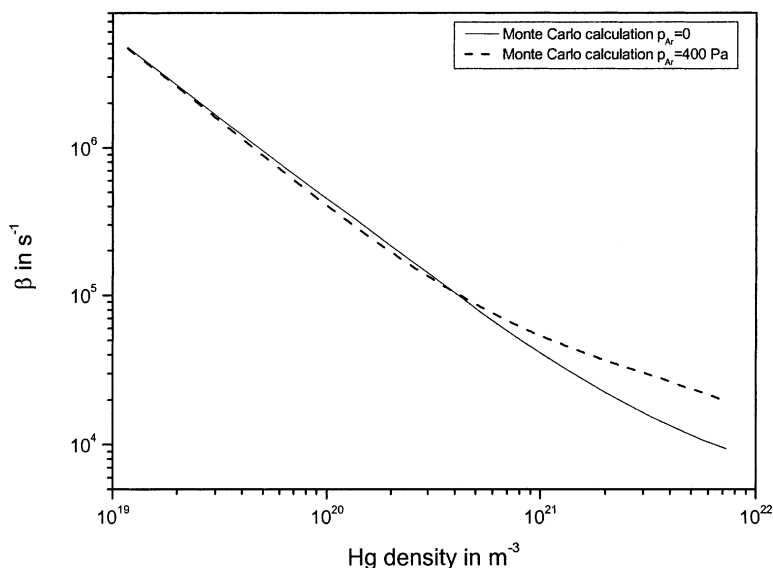
Fig. 3. Effective decay rate of the 6^3P_1 level as a function of the Hg number density. The solid and dashed lines represent the Monte Carlo calculations for a radius R = 12.5 mm with no buffer gas (solid) and with 400 Pa Ar (dashed).

lying within the most intervals. The collisional data applied are the same as in Ref. 10 except the rate constant for $Hg(6^1P_1) + Hg(6^1S_0)$ quenching. Our calculations have shown that a better agreement between the radiation trapping simulation and experimental results from Refs. 10 and 27 can be achieved with a rate constant of 1×10^{-16} m^3/s, rather than with 3×10^{-17} m^3/s, as given in Ref. 10.

Figure 5 shows the calculated decay rate of the 6^1P_1 level as a function of the mercury number density in the cases of 0, 133, and 400 Pa foreign gas (Ar) pressure for a tube radius of 12.5 mm. The results are compared with experimental data from Ref. 27 corresponding to the cases considered. The behavior of the decay rate of the 6^1P_1 level is significantly different from that of the 6^3P_1 level. It shows a pronounced minimum near a Hg number density of about 2×10^{20} m^{-3} (coldest spot temperature 40°C) in the case of no buffer gas. This means that the effective decay rate of the 6^1P_1 level depends not only on the absorption coefficient and its profile but also on the contribution of the resonance dephasing collisions. Beyond the critical density marked, mentioned above, these collisions become important. When buffer gas is present the lineshape is additionally broadened and excitation transfer across the hyperfine components of odd isotopes takes place.
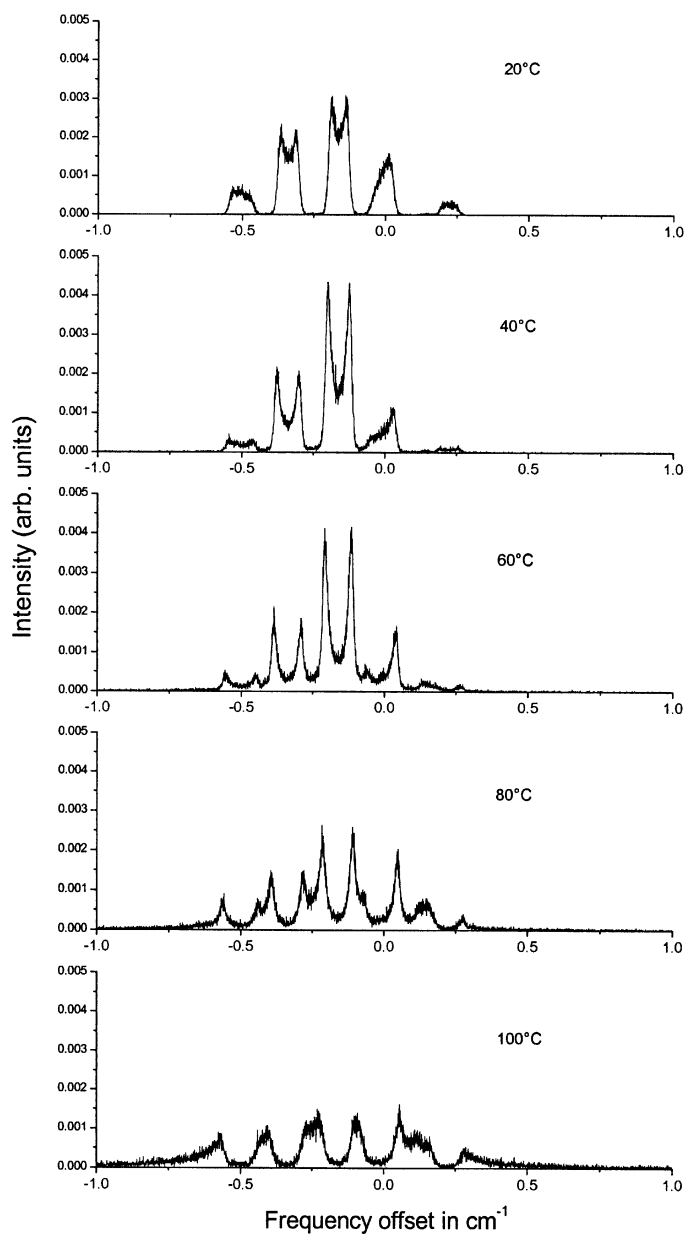
Fig. 4. Calculated spectra of Hg ($6^3P_1 \rightarrow 6^3P_0$) photons escaping from the tube with a radius of 12.5 mm for different coldest spot temperatures. The number of photons launched in each case was 10^5.
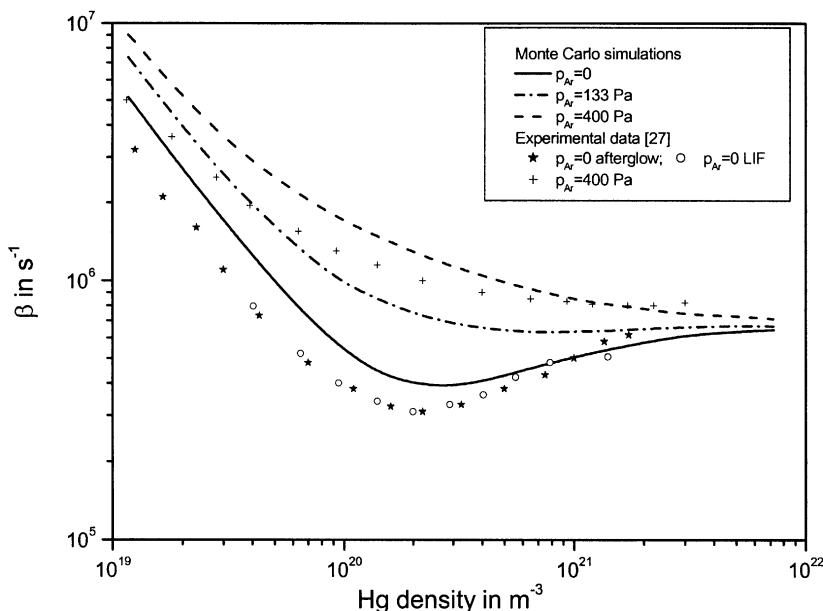
Fig. 5. Calculated effective decay rate of the 6^1P_1 level as a function of the Hg number density for a radius R = 12.5 mm with no buffer gas, and with 100 and 400 Pa Ar. The results are compared with experimental data from Ref. 27.

As a result the effective decay rate increases and the minimum in the decay rate curve disappears.

Figure 6 shows the emission spectra of the 184.9 nm line for various coldest spot temperatures (Hg number densities). In contrast to the previous case (Fig. 4) the hyperfine structure is evident only in the lineshapes corresponding to coldest spot temperatures of 20°C and 40°C. It does no play such a significant role in the radiation trapping of the 184.9 nm resonance line.

4. DENSITIES OF THE EXCITED STATES OF HG AND ESTIMATION OF THE UV OUTPUT

In order to estimate the uv output of the argon–mercury discharge the absolute number densities of the levels 6^3P_1 and 6^1P_1 must be determined. For that purpose we consider a set of balance equations for the 6^3P_0, 6^3P_1, 6^3P_2, and 6^1P_1 states of mercury (see Fig. 1). Assuming stationary conditions
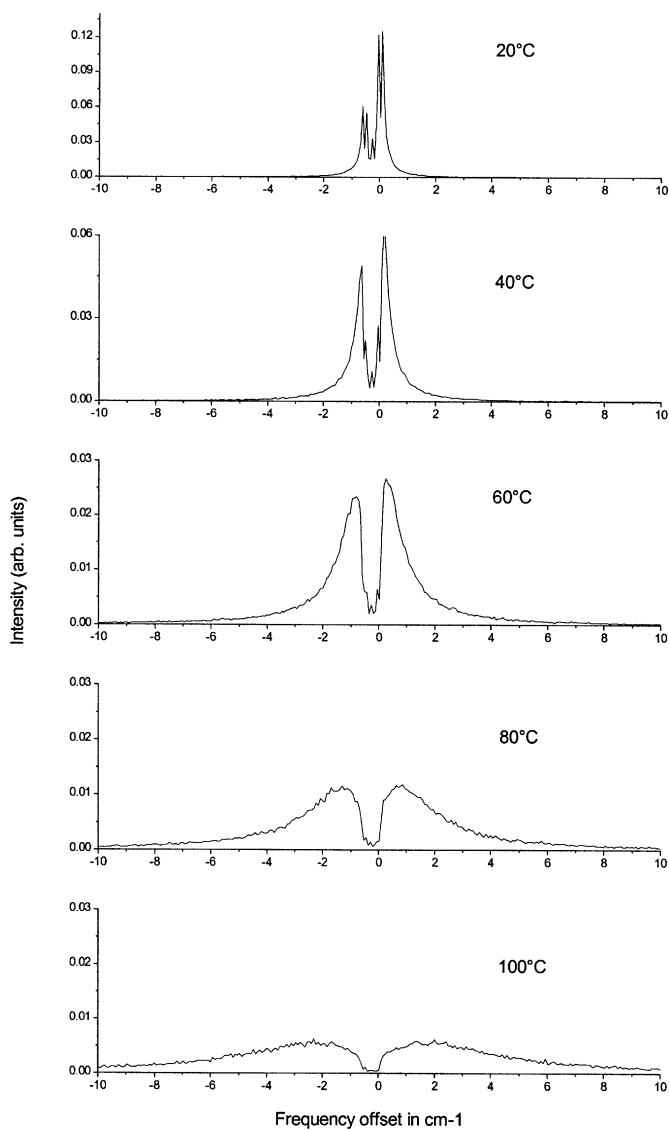
Fig. 6. Calculated spectra of Hg($6^1P_1 \rightarrow 6^3S_0$) photons escaping from the tube with a radius of 12.5 mm for different coldest spot temperature. The number of photons launched in each case was 10^5.

the equations can be written as follows:[(32)]

$$n_e(N_1K_{12} - N_2K_2 + N_3K_{32} + N_4K_{42} + N_5K_{52}) + N_3N_6K_{q3} = 0$$

$$n_e(N_1K_{13} + N_2K_{23} - N_3K_3 + N_4K_{43} + N_5K_{53})$$
$$- N_3(R_{31} + N_6K_{q3}) + N_5(N_6K_{q5a} + N_1K_{q5h}) = 0$$

$$n_e(N_1K_{14} + N_2K_{24} + N_3K_{34} - N_4K_4 + N_5K_{54}) = 0$$

$$n_e(N_1K_{15} + N_2K_{25} + N_3K_{35} + N_4K_{45} - N_5K_5)$$
$$- N_5(R_{51} + N_6K_{q5a} + N_1K_{q5h}) = 0$$

$$(5)$$

where n_e denotes the electron density, N_i $(i = 1 \ldots 5)$ is the density of level i (see Fig. 1), N_6 is the number density of Ar, and K_{ij} are the rate coefficients of transitions $i \rightarrow j$ due to collisions with electrons. R_{31} and R_{51} are the decay rates (denoted as β in the chapter above) of the levels 6^3P_1 and 6^1P_1, respectively, due to resonance radiation. The rate coefficients K_i are given by the following sums:

$$K_2 = \sum_{\substack{j=1 \\ j \neq 2}}^{8} K_{2j}, \quad K_3 = \sum_{\substack{j=1 \\ j \neq 3}}^{8} K_{3j}, \quad K_4 = \sum_{\substack{j=1 \\ j \neq 4}}^{4} K_{4j}, \quad K_5 = \sum_{j=1}^{4} K_{5j} + K_{58}. \quad (6)$$

K_{q3} is the rate coefficient of quenching $6^3P_1 \rightarrow 6^3P_0$, and K_{q5a} and K_{q5h} are the rate coefficients of quenching $6^1P_1 \rightarrow 6^3P_1$ due to collisions with Ar and ground state Hg atoms, respectively. The rate coefficient of quenching K_{q3} is calculated by means of the cross-section of quenching (see Chapter 3.1), and K_{q5a} and K_{q5h} have the values used in the Monte Carlo simulation (see Chapter 3.2). Note that terms accounting for quenching were not considered in Ref. 32. Our calculations have shown that a better agreement with experimental data can be achieved when quenching is included.

To simplify the solution we consider the density of the ground state mercury atoms N_1 and the argon density N_6 as constant across the discharge tube. N_1 is determined by the wall temperature T_w whereas n_e, $N_2 \ldots N_5$ are taken as distributed according to the zeroth-order Bessel function,[29] i.e.,

$$n_i(r) = n_{i0}J_0(2.405r/R) \quad (7)$$

with R–the tube radius and n_{i0} is the corresponding value on the discharge axis. Furthermore we average over the discharge radius. The average value of n_i is given by $\overline{n_i} = 0.432n_{i0}$ and $\overline{n_in_j} = 0.27n_{i0}n_{j0}$. Then we get the profile factor

$$k_b = \frac{\overline{n_in_j}}{\overline{n_i} \cdot \overline{n_j}} \approx 1.45 \quad (8)$$

and can rewrite the global set of rate equations into the form

$$\frac{1}{k_b}N_1K_{12} - N_2K_2 + N_3\left(K_{32} + \frac{N_6}{n_ek_b}K_{q3}\right) + N_4K_{42} + N_5K_{52} = 0$$

$$\frac{1}{k_b}N_1K_{13} + N_2K_{23} - N_3\left(K_3 + \frac{R_{31} + N_6K_{q3}}{k_bn_e}\right)$$

$$+ N_4K_{43} + N_5\left(K_{53} + \frac{N_6K_{q5a} + N_1K_{q5h}}{k_bn_e}\right) = 0$$

$$\frac{1}{k_b}N_1K_{14} + N_2K_{24} + N_3K_{34} - N_4K_4 + N_5K_{54} = 0$$

$$\frac{1}{k_b}N_1K_{15} + N_2K_{25} + N_3K_{35} + N_4K_{45} - N_5\left(K_5 + \frac{R_{51} + N_6K_{q5a} + N_1K_{q5h}}{k_bn_e}\right) = 0$$

$$(9)$$

with n_e, $N_2 \ldots N_5$ now being the averaged number densities. Equation (9) yields $N_2 \ldots N_5$ or given N_1, N_6, and n_e if the rate coefficients K_{ij} are known. These coeficients can be obtained from the cross-sections by integrating over the electron energy distribution function (EEDF). For that purpose we solve the Boltzmann equation for the electrons for a stationary and homogeneous case. We apply the well known two term-expansion of the EEDF (Lorentz approximation)[33] and account for the processes shown in Fig. 1, the most important collisions between electrons and Ar atoms, and e–e collisions. The cross-section data for momentum transfer in elastic collisions with ground state Hg atoms are taken from Ref. 35. Data for excitation of electronic states and direct ionization of the ground state atoms are from Ref. 36. Cross-sections for excitation of excited Hg atoms from Ref. 37 (see also Ref. 32). The cross-sections for superelastic collisions are calculated by using the Klein–Rossenland relation, and those for electron impact ionization of the excited atoms are determined after.[38]

To find the coupled solution for the EEDF and of the balance equations 9 we applied an iterative approach. Starting with a solution of the Boltzmann equation with a reduced electric field E/N (N—the total number density) and electron density derived from experimental data (e.g., Ref. 26), Ar-ground state Hg mixture composition, we obtain the rate coefficients K_{ij} needed to solve the system (9). The solution of Equation (9) provides the densities $N_2 \ldots N_5$. Then we solve the Boltzmann equation again accounting now for the excited states densities $N_2 \ldots N_5$. So, we calculate improved rate coefficients K_{ij}. This procedure is repeated until the values of $N_2 \ldots N_5$ have converged. With the calculated densities of N_3 and N_5 and the effective lifetimes $\tau_{eff,3(5)}$ of the levels 6^3P_1 and 6^1P_1 known from the Monte Carlo

simulation we determine the uv outputs $L_{3(5)}$ of the discharge corresponding to the 253.7 nm and 184.9 nm resonance lines as

$$L_{3(5)} = \frac{N_{3(5)}}{\tau_{eff,3(5)}} e U_{1,3(5)} \pi R^2, \tag{10}$$

where $U_{1,3(5)}$ denotes the respective threshold energy in eV.

The calculations are performed for a mercury–argon discharge (tube radius R = 18 m, discharge current I = 0.4 A, buffer gas pressure p_{Ar} = 400 Pa). Figure 7 shows the values of the averaged electron number density n_e, and the reduced electric field E/N as adopted from Ref. 26 used for the calculations. The densities of the levels 6^3P_1 and 6^1P_1 calculated from Eq. (9) are presented in Fig. 8 in comparison with the respective number densities in Ref. 39 that have been averaged appropriately.

The uv outputs calculated from Ref. 10 are shown in Fig. 9. The results obtained are compared with measured data from Ref. 40. It can be seen that in general the calculated values follow the experimental observations. The radiation output at 253.7 nm shows a maximum for wall temperatures between 30 and 40°C, and decreases at higher temperature values in agreement with the experimental observations.
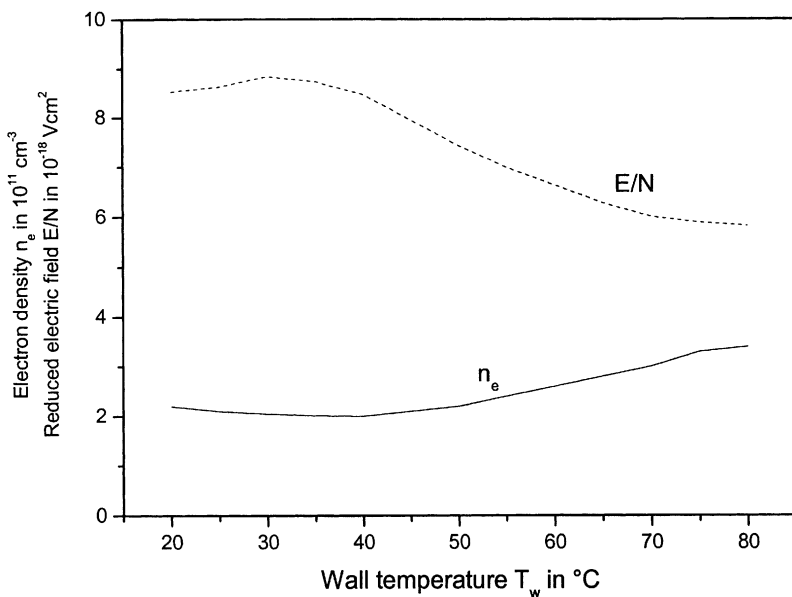

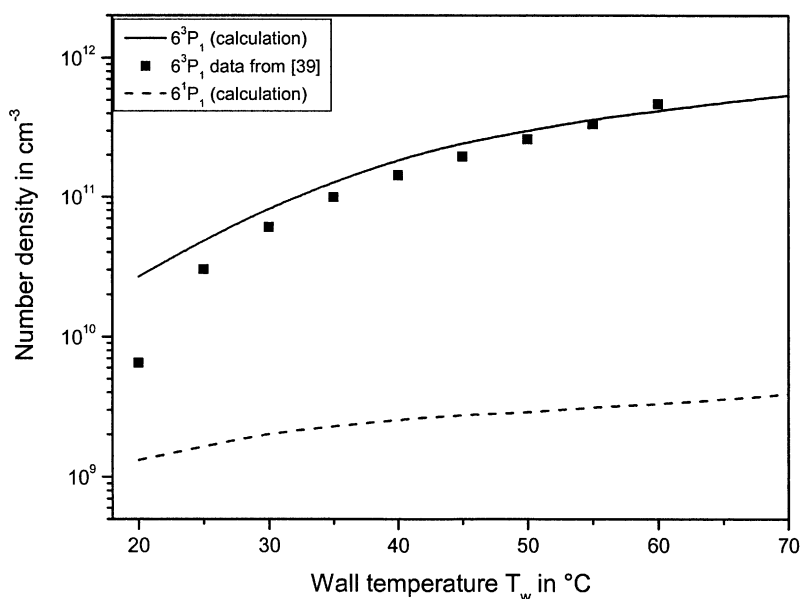**Fig. 7.** Electron density and reduced electric field used in the calculations.

Fig. 8. Calculated population densities of the levels 6^3P_1 (solid) and 6^1P_1 (dash) in Hg–Ar discharges with a tube radius of 18 mm, Ar pressure of 400 Pa, discharge current of 0.4 A. The results are compared with data from Ref. 39.

We were able to achieve a good agreement between calculated and experimental values with this model due to the assumpion of a given electron density. A consistent evaluation of the electron density requires a description of the discharge in more detail (see e.g. Refs. 41, 42). So, the stepwise ionization of mercury, excitation of argon, diffusion of charged particles etc. should be considered. Such extended approach is out of the scope of this work. Our item was to illustrate the application of the results of the Monte Carlo simulation to the estimation of the uv output of fluorescent lamps.

5. CONCLUSION

In this paper the results from Monte Carlo simulation of the trapping of the resonance lines (253.7 nm and 184.9 nm) of mercury in low pressure Hg–Ar discharges have been presented. The hyperfine structure, the isotopic composition, collisional transfers of excitation, foreign gas collisions, and quenching have been considered to achieve a more realistic picture of the
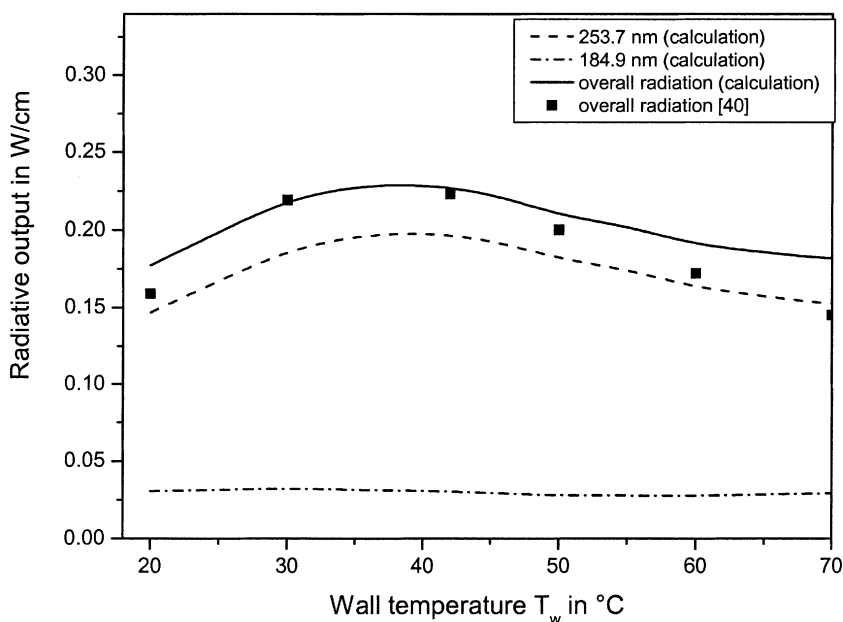
Fig. 9. Calculated radiative outputs of a Hg–Ar discharge (R = 18 mm, p_{Ar} = 400 Pa, I = 0.4 A).

physical processes. The emission spectra and the effective decay rates (lifetimes) of the levels Hg 6^3P_1 and 6^1P_1 have been obtained under conditions typical for the fluorescent lamp operation. The populations of the Hg 6^3P_1 and 6^1P_1 levels have been determined by means of a simple model based on balance equations for the Hg 6^3P_0m, 6^3P_1, 6^3P_2, and 6^1P_1 excited states, and the uv radiation output of the discharge has been estimated for a tube radius of 18 mm, argon pressure of 400 Pa, discharge current 0.4 A, and wall temperatures of 20°C up to 80°C. The results have been found in good agreement with available experimental data.

ACKNOWLEDGMENT

REFERENCES

1. A. F. Molisch and B. P. Oehry, *Radiation Trapping in Atomic Vapours*, Clarendon Press, Oxford (1998).

2. L. M. Biberman, *Zh. Eksp. Teor. Fiz.* **17**, 416–432 (1947).
3. T. Holstein, *Phys. Rev.* **72**, 1212–1233 (1947); *Phys. Rev.* **83**, 1159–1168 (1951).
4. M. G. Payne, J. E. Talmage, G. S. Hurst, and E. B. Wagner, *Phys. Rev. A* **9**, 1050–1069 (1974).
5. H. A. Post, *Phys. Rev. A* **33**, 2003–2016 (1986).
6. J. B. Anderson, J. Maya, M. W. Grossman, R. Lagushenko, and J. F. Waymouth, *Phys. Rev. A* **31**, 2968–2975 (1985).
7. H. M. Anderson, S. D. Bergeson, D. A. Doughty, and J. E. Lawler, *Phys. Rev. A* **51**, 211–217 (1995).
8. T. J. Sommerer, *J. Appl. Phys.* **74**, 1579–1589 (1993).
9. A. C. G. Mitchel and M. W. Zemansky, *Resonance Radiation and Excited Atoms*, Univ. Press, Cambridge (1971).
10. K. L. Menningen and J. E. Lawler, *J. Appl. Phys.* **88**, 3190–3197 (2000).
11. E. D. Cashwell and C. J. Everett, *A Manual of the Monte Carlo Method for Random Walk Problems*, Pergamon Press, New York (1959).
12. A. Corney, *Atomic and Laser Spectroscopy*, Clarendon Press, Oxford (1977).
13. H. R. Griem, *Principles of Plasma Spectroscopy*, University Press, Cambridge (1997).
14. G. Traving, *Über die Theorie der Druckverbreiterung von Spektrallinien*, Braun, Karlsruhe (1960).
15. A. Unsöld, *Physik der Sternatmosphären*, Springer, Berlin (1968).
16. J.-S. Lee, *Astrophys. J.* **192**, 465–473 (1974).
17. J.-S. Lee, *Astrophys. J.* **218**, 857–865 (1977).
18. J.-S. Lee, *Astrophys. J.* **255**, 303–306 (1982).
19. H. R. Skullerud, *J. Phys. D: Appl. Phys.* **1**, 1567–1568 (1968).
20. J.-S. Lee, *Astrophys. J.* **187**, 159–161 (1974).
21. N. E. Holden, R. L. Martin, and I. L. Barnes, *Pure Appl. Chem.* **56**, 675–694 (1984).
22. *CRC Handbook of Chemistry and Physics*, D. R. Lide, ed., CRC Press, Boca Raton (1992).
23. P. Bisling, J. Dederichs, B. Neidhart, and C. Weitkamp, *Fresenius J. Anal. Chem.* **364**, 79–86 (1999).
24. E. Leboucher, C. Bousquet, and N. Bras, *Nouv. Rev. Opt.* **5**, 121–128 (1974).
25. S. Gerstenkorn, J. J. Labarthe, and J. Verges, *Physica Scripta* **15**, 167–172 (1977).
26. W. Verweij, Thesis, University of Utrecht, Philips Res. Rep. Suppl. **2**, 1 (1961).
27. H. A. Post, P. van de Weijer, and R. M. M. Cremers, *Phys. Rev. A* **33**, 2017–2024 (1986).
28. P. van de Weijer and R. M. M. Cremers, *J. Appl. Phys.* **57**, 672–677 (1985).
29. *CRC Handbook of Chemistry and Physics*, D. R. Lide, ed., CRC Press, Boca Raton (1994).
30. L. O. Olsen, *Phys. Rev.* **60**, 739–742 (1941).
31. J. Maya and R. Lagushenko, in *Advances in Atomic, Molecular, and Optical Physics* **26**, 321–373, Academic Press, San Diego (1990).
32. R. B. Winkler, J. Wilhelm, and R. Winkler, *Ann. Physik* **40**, 90–118 (1983).
33. Y. P. Raizer, *Gas Discharge Physics*, Berlin, Springer (1991).
34. M. N. Rosenbluth, W. M. MacDonald, and D. L. Judd, *Phys. Rev.* **107**, 1–6 (1957).
35. J. P. England and M. T. Elford, *Aust. J. Phys.* **44**, 647–675 (1991).
36. S. T. Rockwood, *Phys. Rev. A* **8**, 2348–2358 (1973).
37. C. Kenty, *J. Appl. Phys.* **21**, 1309–1318 (1950).
38. L. Vriens, R. A. J. Keijser, and F. A. S. Ligthart, *J. Appl. Phys.* **49**, 3807–3813 (1978).
39. M. Koedam and A. A. Kruithof, *Physica* **28**, 80–100 (1962).
40. M. Koedam, A. A. Kruithof, and J. Riemens, *Physica* **29**, 565–584 (1963).
41. G. Zissis, P. Benetruy, and I. Bernat, *Phys. Rev. A* **45**, 1135–1149 (1992).
42. G. G. Lister and S. E. Coe, *Comp. Phys. Commun.* **75**, 160–184 (1993).